Atomically dispersed Zn stabilized $Ni^{\delta+}$ enabling tunable selectivity for CO_2 hydrogenation

Yaning Wang[#[a]], Kai Feng[#[a]], Jiaming Tian[[a]], Jiajun Zhang[[b]], Baohuai Zhao[[c]], Kai Hong Luo[[d]], Binhang Yan[*[a]]

[a] *Y. Wang, K. Feng, J. Tian, Prof. B. Yan*

Department of Chemical Engineering, Tsinghua University, Beijing 100084, China

Email: binhangyan@tsinghua.edu.cn

[b] *J. Zhang*

Department of Energy and Power Engineering, Tsinghua University, Beijing 100084, China

[c] *B. Zhao*

Institute of Engineering Technology, SINOPEC Catalyst Co., Ltd, Beijing 101111, China

[d] *Prof. K. Luo*

Department of Mechanical Engineering, University College London, Torrington Place, London WC1E 7JE, UK

[#] *Y. Wang and K. Feng contributed equally to this work.*

Abstract

For a heterogeneous catalytic process, the catalytic performance of catalysts could be improved by modifying the active metal with a second element. Determining the enhanced mechanism of the second element is essential to the rational design of catalysts. In this work, Zn as a second element was introduced into Ni/ZrO_2 for CO_2 hydrogenation. Compared to Ni/ZrO_2, the selectivity of $NiZn/ZrO_2$ was observed to shift from CH_4 to CO. A series of structural characterization results revealed that Zn was atomically dispersed in the phase of NiO and ZrO_2 in the form of $NiZnO_x$ and $ZnZrO_x$ during CO_2 hydrogenation, stabilizing higher valence state of Ni ($Ni^{\delta+}$) under hydrogenation atmosphere over Ni-O-Zn site and thus promoting the generation of CO. These findings shed light on an O-mediated bimetallic effect of $NiZn/ZrO_2$ and bring new insight into the rational design of more efficient heterogeneous catalysts.

Introduction

It is of long-standing interest to improve the activity and selectivity of heterogeneous catalytic processes, which also represents a challenge for the rational design of heterogeneous catalysts.[1] Transition metal catalysts, represent a most successful class of heterogeneous catalyst, have been widely used in many chemical industries.[2] In a catalytic process, the transition metal usually plays as the active site to drive the catalytic reaction, while the catalytic performance in principle depends on the electronic structure of the active metal because it determines the adsorption and desorption of the intermediate species.[3] However, it is difficult to balance the adsorption and desorption of the intermediate species described by Sabatier's principle over the intrinsic electronic structure of active metals.[4] Therefore, it is necessary to modify the electronic structure of the active metal for optimizing the catalytic performance.[5]

Introducing second metals including alkali metals, [6] rare earth metals, [7] and transition metals[8] as modifiers, is an efficient strategy to modify the electronic structure of the active metal over a bimetallic effect. Alloys or intermetallic compounds are a typical bimetallic system, in which charge transfer occurs between the active metal and the modifier metal due to the difference in their electronegativity.[9] For example, it was found that the active Pd in PdIn alloys exhibits a slight negative charge due to the electron transfer from In to Pd and thus improves the ethylene selectivity during the semi-hydrogenation of acetylene due to the weakened adsorption of ethylene on $Pd^{\delta-}$.[10] However, this electronegativity-related electron transfer law between two metals is being challenged due to the possible introduction of O element with high electronegativity into the bimetallic system.[11] Qin et al. found that the modification of alkali metals (e.g., Na) on catalysts stabilizes the ligand O of the active metal

Ru under hydrogenation atmosphere rather than directly transferring electrons to Ru, suppressing the reduction and aggregation of single Ru atom sites and thus improving the reaction stabilization.[6a] Moreover, Xie et al. also found that the PdFe alloy is changed to Pd-rich PdFe alloy and FeO_x during the CO_2-assisted C_2H_6 dehydrogenation process due to the existence of the oxidant CO_2, and the resulting interfacial Pd-O-Fe as a synergistic catalytic site ultimately increases ethylene selectivity.[12] This M_1-O-M_2 interfacial active site constructed by the introduction of a second metal (M_2) has also been widely used to explain the improved catalytic performance.[13] These studies provide a new concept of O-mediated bimetallic effect, but also bring a new challenge to identify the role of interfacial O during catalytic processes, as a synergistic catalytic site or affecting the electronic structure of the active metal due to high electronegativity.

Here, Zn was introduced into Ni/ZrO_2 catalysts to illustrate the role of interfacial O in tuning CO_2 hydrogenation activity and selectivity. Compared with catalysts without Zn, the addition of Zn significantly shifted the selectivity of the catalysts from CH_4-favored to CO-favored. A series of structural characterization results indicated that the introduced Zn was atomically dispersed in the catalyst in the form of $NiZnO_x$ and $ZnZrO_x$, respectively. Furthermore, the *in-situ* diffuse reflection infrared Fourier transform spectroscopy (DRIFTS) results and density functional theory (DFT) calculations suggested that the Ni-O-Zn coordination stabilizes the electronic structure of $Ni^{\delta+}$ during CO_2 hydrogenation, weakening the hydrogenation ability of absorbed CO and promoting the generation of CO. This work reveals the O-mediated bimetallic effect on CO_2 hydrogenation process and provides a new chance for stable modulation of the electronic structure of active metals.

Results and Discussion

Catalytic performance evaluation.

The catalytic reaction of CO_2 hydrogenation at 400 ℃ with a gas hourly space velocity (GHSV) of 24 000 $ml \cdot g^{-1} \cdot h^{-1}$was performed over Ni/ZrO_2, Zn/ZrO_2 and $NiZn/ZrO_2$ catalysts. As shown in **Figure 1a** and **Table 1**, Ni/ZrO_2 typically favors the CO_2 methanation process with high CO_2 conversion and CH_4 selectivity. In contrast, the introduction of Zn into Ni/ZrO_2 (i.e., $NiZn/ZrO_2$) significantly shifts the product selectivity from CH_4 to CO. This means that the reverse water gas shift (RWGS) reaction dominates the CO_2 hydrogenation process. Although the CO_2 conversion decreases with the addition of Zn, the yield of CO is improved remarkably compared with Ni/ZrO_2 (**Table 1**). Meanwhile, when the CO_2 conversion of Ni/ZrO_2 (22.7%) is controlled at a similar level to that of $NiZn/ZrO_2$ (20.1%), the CH_4 selectivity of Ni/ZrO_2 still keeps a relatively high value of 73.7% (**Table 1**). Moreover, Zn/ZrO_2 also shows a high CO selectivity but poor CO_2 conversion, indicating the generation of CO for $NiZn/ZrO_2$ should be attributed to the modification of Ni by the addition of Zn. Compared to the NiZn-based catalysts reported previously in **Table S1**, $NiZn/ZrO_2$ in this work shows enhanced CO selectivity and yield. To figure out the effect of Zn, Ni/ZnO, $Ni/ZnZrO_x$, physical mixed Ni/ZrO_2 and Zn/ZrO_2 (labeled as Ni/ZrO_2+Zn/ZrO_2) were also tested as the references and the results are displayed in **Figure S1**. In contrast with the high CH_4 selectivity over Ni/ZrO_2+Zn/ZrO_2 and the low CO_2 conversion over Ni/ZnO, $Ni/ZnZrO_x$ exhibits similar activity and selectivity to $NiZn/ZrO_2$. Furthermore, CO_2 hydrogenation at various temperatures (360-400 ℃) was also carried out for the three catalysts. It is found that the CO_2 conversion of all three catalysts increases with increasing reaction temperature, while the product selectivity

is almost unchanged (**Figure 1b**). The results of steady-state reaction over 14 h also indicate that the selectivity shift of Ni/ZrO_2 induced by the modification of Zn is stable (**Figure 1c**). Moreover, catalytic tests with different feed gas ratio were also performed and the results are displayed in **Table S2**. $NiZn/ZrO_2$ maintains high selectivity towards CO with different CO_2:H_2 ratio. $NiZn/ZrO_2$ exhibits poor activity for CO hydrogenation, demonstrating that the conversion of CO into CH_4 is inhibited over $NiZn/ZrO_2$. These results indicate that the addition of Zn into Ni/ZrO_2 could significantly tune the product selectivity of CO_2 hydrogenation, which is consistent with the previous report.[14]

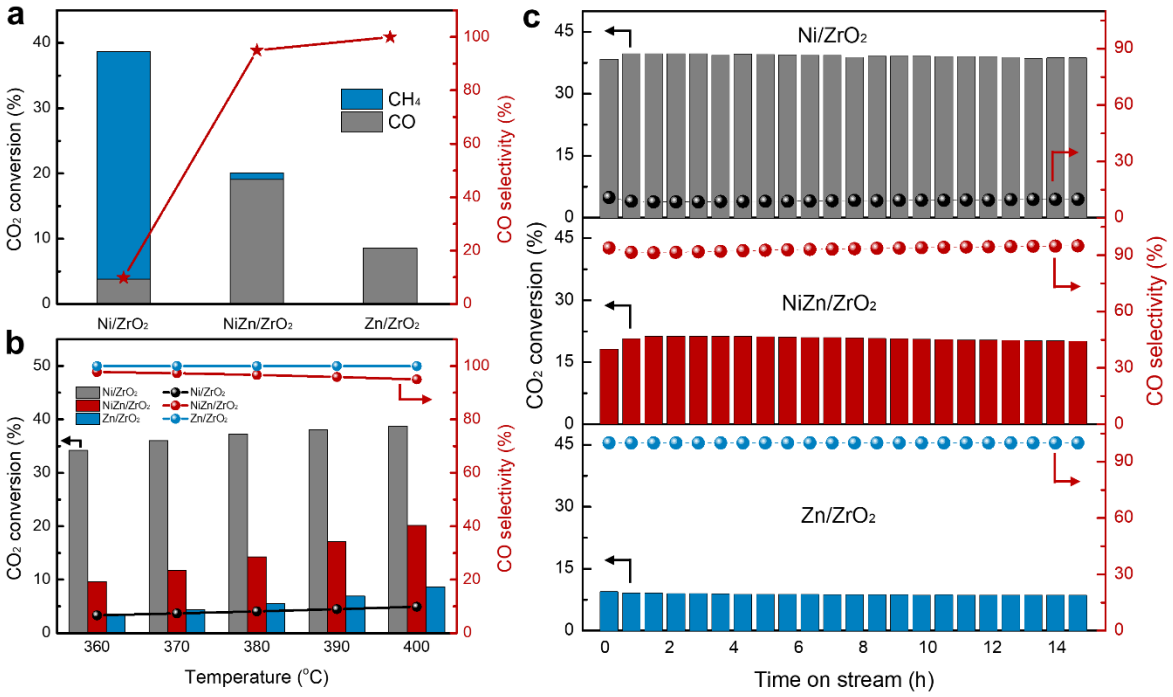

Figure 1 CO_2 conversion and CO selectivity of Ni/ZrO_2, $NiZn/ZrO_2$ and Zn/ZrO_2 catalysts for CO_2 hydrogenation at (a) 400 °C and (b) different temperatures from 360-400 °C. (c) Catalytic performances of the three catalysts in long-term stability test for 14 h at 400 °C.

Table 1 CO_2 hydrogenation performance of Ni/ZrO_2, $NiZn/ZrO_2$ and Zn/ZrO_2 catalysts at 400 °C (calculated by averaging data points between 12 and 14 h on stream, $CO_2/H_2/Ar$ = 5/10/25 mL·min^{-1})

Catalyst	CO_2 conversion (%)	Selectivity (%)		Yield (%)	
		CO	CH_4	CO	CH_4
Ni/ZrO_2[a]	38.7	9.8	90.2	3.8	34.9
$NiZn/ZrO_2$[a]	20.1	95.0	5.0	19.1	1.0
Zn/ZrO_2[a]	8.6	100	0	8.6	0
Ni/ZrO_2[b]	22.7	26.3	73.7	6.0	16.7

[a] 100 mg catalyst, [b] 10 mg catalyst + 90 mg SiO_2.

Structural evolution of Ni caused by introducing Zn.

To investigate the origin of shifted products selectivity, a series of structural characterization was carried out for Ni/ZrO_2 and $NiZn/ZrO_2$ catalysts. **Figure 2a** shows the X-ray diffraction (XRD) patterns of fresh and spent Ni/ZrO_2 and $NiZn/ZrO_2$ catalysts, in which two characteristic peaks at 5.7° and 6.6° are assigned to the (111) and (200) orientation of cubic NiO (PDF-#89-7130) respectively. Notably, these two characteristic peaks in fresh $NiZn/ZrO_2$ show a slight shift to lower 2θ values from 6.60° and 5.71° to 6.58° and 5.69° compared to those in fresh Ni/ZrO_2, implying the penetration of Zn into NiO (denote as $Ni_{1-x}Zn_xO$). Based on the linear relationship between Zn content and the lattice parameter of $Ni_{1-x}Zn_xO$, it could be inferred that $Ni_{0.8}Zn_{0.2}O$ (PDF-#75-0271) is formed in the fresh $NiZn/ZrO_2$ catalyst.[15] The grain size of NiO and $Ni_{0.8}Zn_{0.2}O$ in the two fresh catalysts are determined to be ~11 and ~14 nm through the Scherrer equation, respectively (**Table S3**). Moreover, apart from the characteristic peaks of ZrO_2, the (102) peak of hexagonal ZnO (PDF-#80-0074) at 7.2° is also observed, which should be attributed to the residual Zn species that do not interact with NiO. After CO_2 hydrogenation reaction, it is found that the characteristic peaks of NiO in spent

Ni/ZrO_2 disappear, while the (111) peak of metallic Ni (PDF-#70-0989) at 7.9° is observed, indicating the reduction of NiO to metallic Ni during CO_2 hydrogenation atmosphere. In contrast, the (200) peak of $Ni_{0.8}Zn_{0.2}O$ in spent NiZn/ZrO_2 further shifts to a lower 2θ value from 6.58° to 6.55° and the (102) peak of ZnO disappears, indicating the residual Zn species further interacts with $Ni_{0.8}Zn_{0.2}O$ and thus results in the formation of $Ni_{0.6}Zn_{0.4}O$ (PDF-#75-0273) during the reaction. The disappearance of the (111) peak of $Ni_{0.8}Zn_{0.2}O$ after reaction might be attributed to that the high-index crystal planes are easier to be reduced. These results indicate that the introduction of Zn enables Ni species to maintain the oxidation state under CO_2 hydrogenation reaction conditions. This conclusion is also directly confirmed by the results of temperature-programmed H_2 reduction (H_2-TPR) for Ni/ZrO_2 and NiZn/ZrO_2, in which the reduction of Ni species in NiZn/ZrO_2 requires a higher reduction temperature than that in Ni/ZrO_2 (**Figure S2**). As previously reported, the electronic structure sensitivity of Ni-based catalysts in CO_2 hydrogenation has been widely unraveled, in which positively charged Ni ($Ni^{\delta+}$) promotes the RWGS process and metallic Ni (Ni^0) facilitates the generation of CH_4.[16] Therefore, the stabilized oxidation state of Ni species in NiZn/ZrO_2 during CO_2 hydrogenation might be the key factor inducing the shift of product selectivity.

To further understand the effect of Zn introduction on the electronic structure of Ni species, X-ray absorption fine structure (XAFS) measurements were carried out. As shown in **Figure 2b**, the X-ray absorption near edge structure (XANES) spectra of fresh Ni/ZrO_2 and NiZn/ZrO_2 show a typical K-edge absorption of NiO, suggesting the existence of Ni^{2+} in the two fresh catalysts. Moreover, **Figure 2c** shows the extended X-ray absorption fine structure (EXAFS) spectra of fresh Ni/ZrO_2 and NiZn/ZrO_2, in which two peaks at 1.6 Å and 2.6 Å corresponding

to the Ni-O and Ni-O-Ni coordination of NiO respectively are observed. According to the fitting results (**Table S4**), the average coordination numbers of Ni-O ($CN_{Ni\text{-}O}$) for fresh Ni/ZrO_2 (5.8±0.5) and NiZn/ZrO_2 (6.4±0.7) are similar while the $CN_{Ni\text{-}O\text{-}Ni}$ of fresh Ni/ZrO_2 (5.9±0.7) is much smaller than that of NiZn/ZrO_2 (10.0±0.9). This suggests that the particle size of NiO in fresh Ni/ZrO_2 is smaller than that in fresh NiZn/ZrO_2, which is also consistent with the XRD results. Furthermore, the *in-situ* XAFS experiments were carried out for Ni/ZrO_2 and NiZn/ZrO_2 to further demonstrate the improved valence-state stability of Ni species due to the introduction of Zn under CO_2 hydrogenation reaction conditions. As shown in **Figure 2d**, both the *in-situ* XANES spectra of Ni/ZrO_2 and NiZn/ZrO_2 show a decrease in the white-line peak height and a red-shift of Ni K-edge compared to the standard NiO sample, indicating the reduction of Ni^{2+} to Ni^0 during the CO_2 hydrogenation process. Notably, Ni species in NiZn/ZrO_2 still present a higher valence state than those in Ni/ZrO_2 under *in-situ* reaction conditions, in which the contents of Ni^{2+} are determined as 23% and 60% for Ni/ZrO_2 and NiZn/ZrO_2 respectively according to the results of linear combination fitting (LCF, **Figure S3** and **Table S5**). These results further demonstrate that the introduction of Zn stabilizes Ni species with a positive charge and improves the reduction resistance of Ni^{2+} during CO_2 hydrogenation.

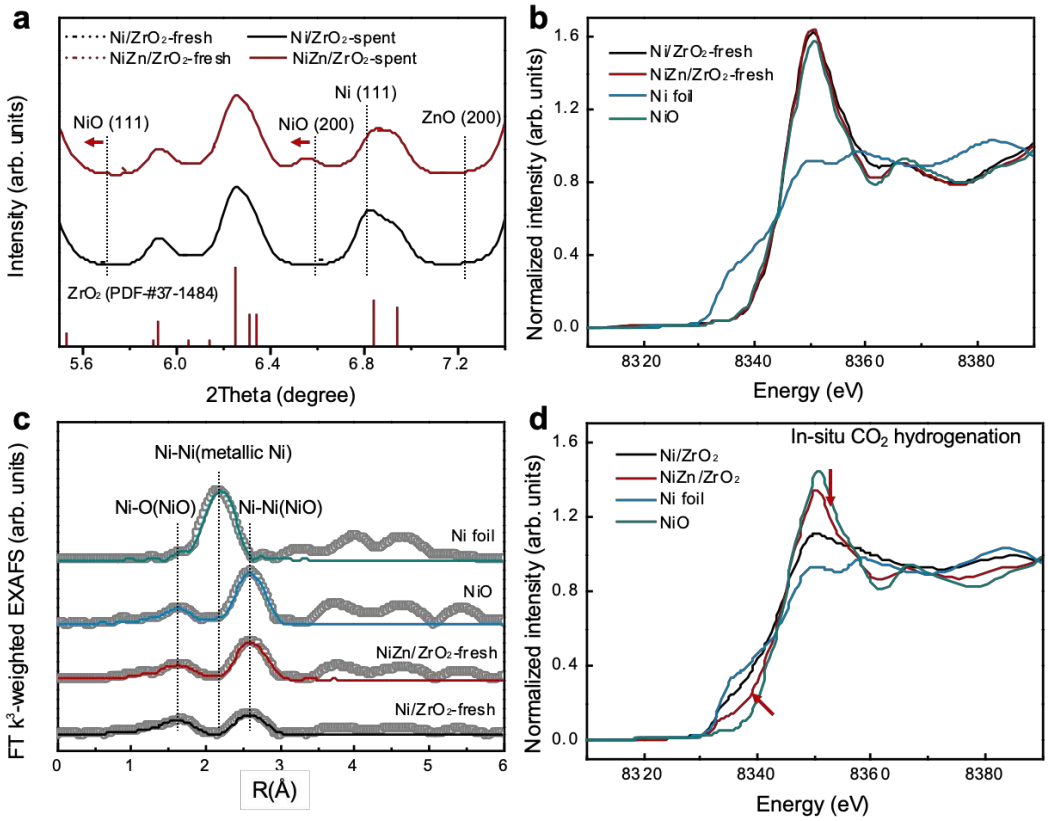

Figure 2 (a) XRD patterns of the fresh and spent Ni/ZrO_2 and NiZn/ZrO_2 catalysts. (b) XANES and (c) EXAFS spectra of the fresh Ni/ZrO_2 and NiZn/ZrO_2 catalysts. (d) *In-situ* XANES spectra of the Ni/ZrO_2 and NiZn/ZrO_2 catalysts.

Structural characterization of Zn in Zn/ZrO_2 and NiZn/ZrO_2.

Furthermore, the transmission electron microscopy (TEM) images of Ni/ZrO_2-fresh, Ni/ZrO_2-spent, NiZn/ZrO_2-fresh, and NiZn/ZrO_2-spent show the size of ZrO_2 nanoparticles is in the range of 10-30 nm, however, it is difficult to identify NiO or Ni nanoparticles in TEM images due to the negligible contrast differentiation between Ni species and ZrO_2 (**Figure S4**). To this end, EDX elemental mappings were used to investigate the dispersion of Ni species on ZrO_2 support. As shown in **Figure 3a**, green aggregated points are observed on the EDX mapping of Ni, representing that Ni species in Ni/ZrO_2-fresh are supported on ZrO_2 as

nanoparticles. After the CO_2 hydrogenation reaction, the Ni species in Ni/ZrO_2-spent still maintain nanoparticle morphology (**Figure 3b**). Green aggregated points are also observed in the EDX Ni mapping of NiZn/ZrO_2-fresh, however, it is found that Ni species are homogeneously distributed on ZrO_2 after CO_2 hydrogenation reaction (**Figure 3c** and **3d**). Meanwhile, further dispersion of Zn species is observed for NiZn/ZrO_2-spent compared to NiZn/ZrO_2-fresh. Since the formation of Zr-based solid solution (e.g., $ZnZrO_x$, $CdZrO_x$ $GaZrO_x$, and $CeZrO_x$) during the reaction has been widely reported for a variety of catalytic processes,[17] these results suggest that apart from the penetration of Zn into NiO, Zn might be also penetrated into ZrO_2 support as $ZnZrO_x$ solid solution and thus promotes the dispersion of Ni species. To further determine the state of Zn species, Zn K-edge XAFS spectra of NiZn/ZrO_2-spent were obtained. As shown in **Figure 3e**, the strong white-line intensity and absorption edge position of Zn similar to the standard ZnO sample are observed, indicating the Zn species in NiZn/ZrO_2 still retain an oxidized state after the reaction. However, it is noted that the white-line peak of NiZn/ZrO_2-spent shows a red-shift compared to ZnO, implying a coordination geometry of Zn atoms different from ZnO. The XANES spectra of Zn/ZrO_2-spent were also obtained as comparison. The similar Zn K-edge feature of Zn/ZrO_2-spent compared to NiZn/ZrO_2-spent further demonstrates that the Zn species in NiZn/ZrO_2 could interact with ZrO_2 support during the reaction. Furthermore, the EXAFS spectra of NiZn/ZrO_2-spent and Zn/ZrO_2-spent are shown in **Figure 3f**. It is found that a strong Zn-O peak at approximately 1.6 Å while no signal of Zn-O-Zn at higher distances is observed for these two catalysts, indicating Zn mainly exists in the form of isolated Zn-O sites. Therefore, based on the above results, it can be concluded that Zn species are atomically dispersed in NiZn/ZrO_2 in the form

of $NiZnO_x$ and $ZnZrO_x$, improving the electronic structure stability of Ni species during CO_2 hydrogenation.

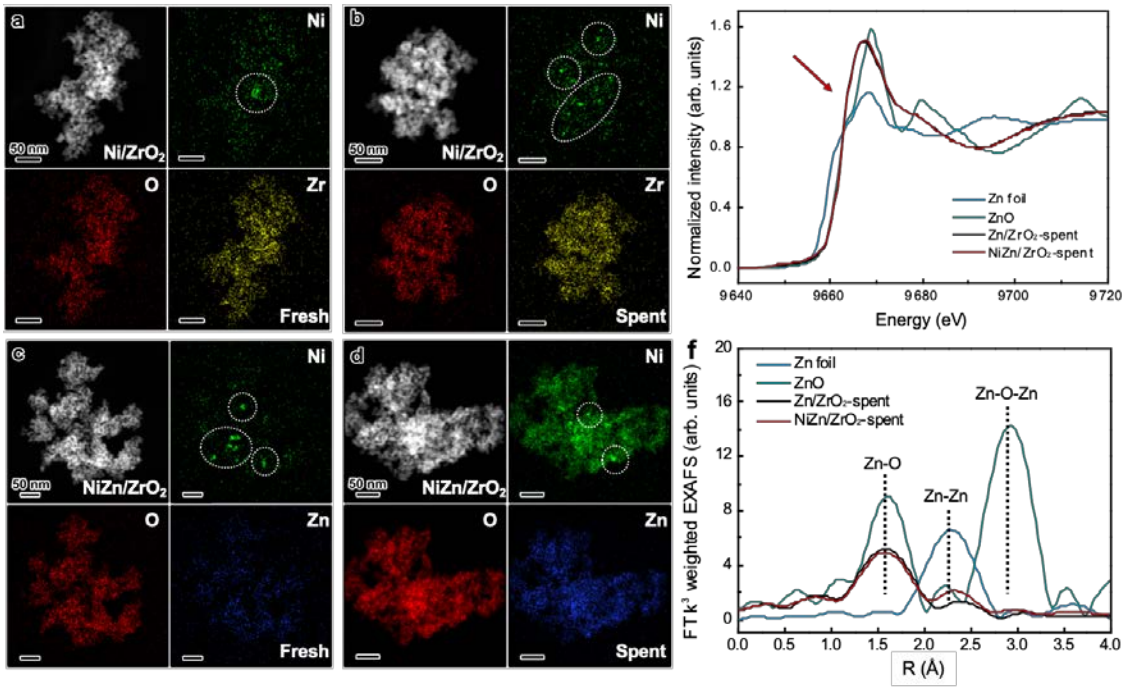

Figure 3 High-angle annular dark field scanning transmission electron microscopy (HAADF-STEM) images and energy dispersive X-Ray spectroscopy (EDX) elemental mappings (Ni in green, O in red, Zr in yellow and Zn in blue) of (a) Ni/ZrO_2-fresh, (b) Ni/ZrO_2-spent, (c) $NiZn/ZrO_2$-fresh, and (d) $NiZn/ZrO_2$-spent. (e) XANES and (c) EXAFS spectra of Zn/ZrO_2-spent and $NiZn/ZrO_2$-spent.

Theoretical insights into the O-mediated bimetallic effect.

To further demonstrate this conclusion by comparing the structure stability of NiO and $NiZnO_x$ under reduction atmosphere, the potential energy for the removal of O atom in Ni-O-Ni and Ni-O-Zn during H_2 reduction was evaluated using DFT calculations, in which NiO and $NiZnO_x$ were modeled by depositing Ni_4O_4 and $Ni_3Zn_1O_4$ clusters on monoclinic ZrO_2, respectively (**Figures 4a** and **4b**). It is found that higher energy is required for the removal of O from Ni-O-Zn (0.77 eV in **Figure 4b**) than from Ni-O-Ni (0.24 eV in **Figure 4a**), which is

consistent with the H_2-TPR results (**Figure S2**). To investigate the origin of the stronger structure stability of Ni-O-Zn, the bonding strengths of O to three ligand atoms (O-Ni_1, O-Ni_2, and O-Ni_3 for Ni_4O_4/ZrO_2; O-Zn_1, O-Ni_2, O-Ni_3 for $Ni_3Zn_1O_4/ZrO_2$) were evaluated through the crystal orbital Hamilton populations (COHPs) analysis. As shown in **Figures 4c** and **4d**, the O-Ni_2 and O-Ni_3 for Ni_4O_4/ZrO_2 show more negative integrated projected COHPs (ICOHPs) values than those for $Ni_3Zn_1O_4/ZrO_2$, indicating that the bonding strength of O-Ni in Ni_4O_4/ZrO_2 is stronger. In contrast, the ICPHPs values of O-Zn_1 (-2.36 eV for spin up and -2.34 eV for spin down) for $Ni_3Zn_1O_4/ZrO_2$ is more negative than those of O-Ni_1 (-2.25 eV for spin up and -1.92 eV for spin down) for Ni_4O_4/ZrO_2, which suggests that although the introduction of Zn weakens the bond strength of Ni-O in Ni-O-Zn, the enhanced Zn-O bond strength still improve the stability of Ni-O-Zn. Therefore, it could be concluded that the introduction of Zn improves the structural stability of Ni-O-Zn, thus improving the bonding strength of Ni to ligand O, which is consistent with the above experimental results.

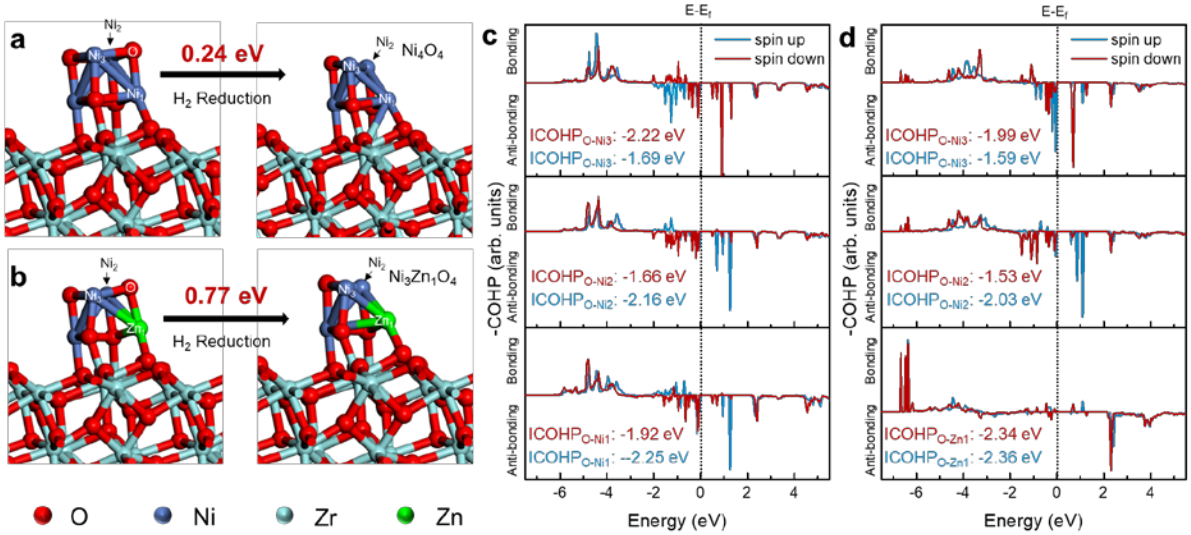

Figure 4 The potential energy and structure illustrations for deoxidation of (a) Ni_4O_4/ZrO_2 and $Ni_3Zn_1O_4/ZrO_2$ during H_2 reduction. Crystal orbital Hamilton populations (COHPs) analysis for three

coordinate bonds of oxygen atoms in (c) Ni_4O_4 and (d) $Ni_3Zn_1O_4$. ($O\text{-}Ni_1$, $O\text{-}Ni_2$, and $O\text{-}Ni_3$ for Ni_4O_4/ZrO_2; $O\text{-}Zn_1$, $O\text{-}Ni_2$, $O\text{-}Ni_3$ for $Ni_3Zn_1O_4/ZrO_2$).

Understanding of the structure-function relationship.

To correlate the relationship between the structure and catalytic performance, *in-situ* DRIFTS combined with transient response experiments of CO_2 hydrogenation were performed. As shown in **Figure 5a** and **5b inset**, three absorbed CO (*CO) peaks are found for Ni/ZrO_2 catalyst during CO_2 hydrogenation, including linear CO adsorption at 2014 cm^{-1} and bridge CO adsorption at 1912 cm^{-1} and 1849 cm^{-1}, while only a linear *CO peak is found at 2027 cm^{-1} for $NiZn/ZrO_2$.[18] Increased wavenumber of linear CO adsorption and absence of bridge CO adsorption for $NiZn/ZrO_2$ suggest that the binding strength of *CO on $NiZn/ZrO_2$ is weaker than that on Ni/ZrO_2. For CO_2 hydrogenation, it is well known that strong adsorption of *CO would result in continuing hydrogenation of *CO species to produce CH_4 while weak adsorption of *CO favors the desorption of CO. Moreover, monodentate carbonate and bidentate formate adsorbed species are also observed for Ni/ZrO_2 and $NiZn/ZrO_2$, representing a possible formate pathway for the generation of CH_4 (**Figures 5a** and **5b**, **Figure S5** and **Table S6**). In addition, *in-situ* DRIFTS experiments were also carried out with the co-feeding of CO and CO_2. As shown in **Figures S5** and **S6**, no significant difference in adsorption behaviors is observed. To further distinguish the effects of different pathways on the generation of CH_4, the hydrogenation ability of these three intermediates was evaluated through CO_2 hydrogenation transient response experiments. As shown in **Figures 5c** and **5d**, after switching the reaction gas from H_2+CO_2 to H_2+N_2 at the reaction temperature, both the normalized intensities of $*CO_3$ and *HCOO show a similar decrease trend for Ni/ZrO_2 and $NiZn/ZrO_2$. In contrast, the

normalized intensity of *CO for NiZn/ZrO_2 shows a much slower decrease trend, in which within 0.5 min after switching the gas, the *CO intensity of Ni/ZrO_2 and NiZn/ZrO_2 is decreased by 96% and 67%, respectively. Therefore, the difference in the selectivity of CO_2 hydrogenation for Ni/ZrO_2 and NiZn/ZrO_2 is mainly determined by the hydrogenation ability of surface *CO on catalysts, in which the *CO on Ni/ZrO_2 is more easily to be hydrogenated to CH_4 than that on NiZn/ZrO_2. Therefore, the modification of Ni/ZrO_2 by the addition of single-site Zn can stabilize the high valence state of Ni under reaction conditions and consequently weaken its adsorption and hydrogenation capacity for *CO, thus reducing the CH_4 selectivity.

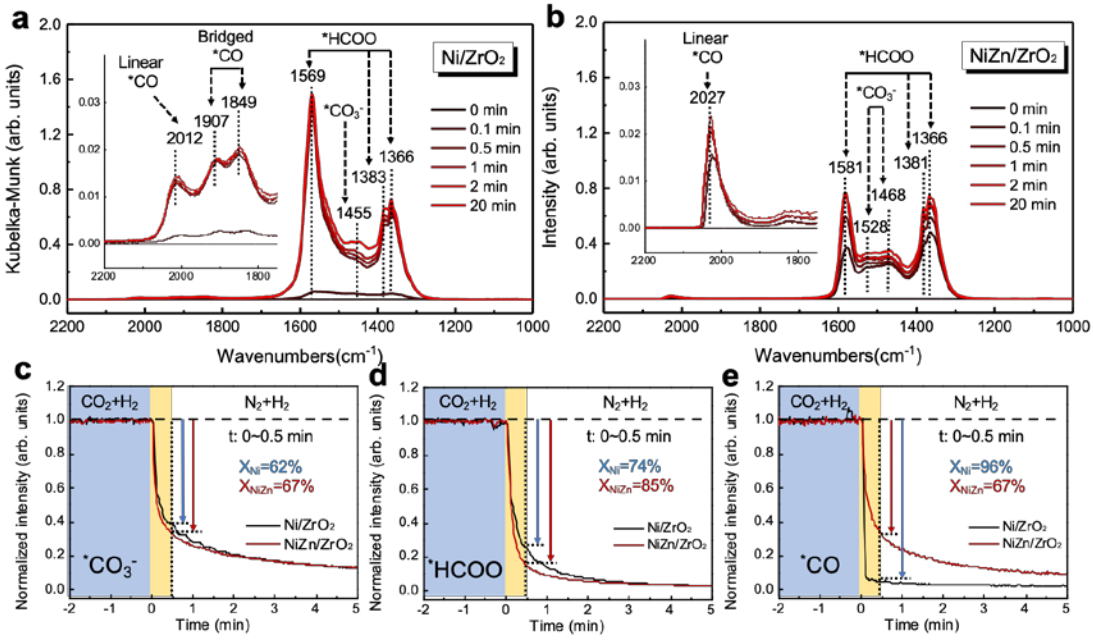

Figure 5 *In-situ* DRIFT spectra of (a) Ni/ZrO_2 and (b) NiZn/ZrO_2 during the CO_2 hydrogenation reaction at 400 °C in the region of 2200-1000 cm^{-1}. The dynamic change of (c) $*CO_3^-$ (1455 cm^{-1} for Ni/ZrO_2, 1468 cm^{-1} for NiZn/ZrO_2), (d) *HCOO (1569 cm^{-1} for Ni/ZrO_2, and 1581 cm^{-1} for NiZn/ZrO_2), and linear *CO (2012 cm^{-1} for Ni/ZrO_2, 2027 cm^{-1} for NiZn/ZrO_2) species signal with time for Ni/ZrO_2 and NiZn/ZrO_2 catalysts during transient response experiments after switching the reaction gas from CO_2+H_2 to N_2+H_2.

Conclusion

The O-mediated bimetallic effect of $NiZn/ZrO_2$ on CO_2 hydrogenation performance was systematically investigated in this work. The introduction of Zn into Ni/ZrO_2 significantly shifts the product selectivity from CH_4 to CO for CO_2 hydrogenation. The introduced Zn is revealed to be atomically dispersed in the phase of the NiO and ZrO_2 in the form of $NiZnO_x$ and $ZnZrO_x$, respectively. The formed Ni-O-Zn sites enhance the strength of Ni-O bonding and stabilize the positive valence state of Ni ($Ni^{\delta+}$) under reaction conditions, weakening the hydrogenation ability of *CO to CH_4 during CO_2 hydrogenation and thus facilitating the RWGS process. Our work brings a new insight into the O-mediated bimetallic effect on the CO_2 hydrogenation process and sheds light on the rational design of more efficient heterogeneous catalysts with fine-tuned product selectivity.

Experimental Section

Synthesis of Catalysts.

Ni/ZrO_2, Zn/ZrO_2, and $NiZn/ZrO_2$ were synthesized by an impregnation method over commercial ZrO_2 support (48-63 m^2/g, Alfa Aesa). Precursor solutions were prepared by dissolving $Ni(NO_3)_2 \cdot 6H_2O$ (99.999%, Sigma Aldrich) and/or $Zn(NO_3)_2 \cdot 6H_2O$ (≥99.0%, Sigma Aldrich). Then the support was added into the solutions and water was evaporated at 70 ℃ under stirring to form a slurry. After drying at 110 ℃ overnight, the samples were calcined in static air at 450 ℃ for 5 h with a heating rate of 1 $℃ \cdot min^{-1}$. The loadings of Ni and Zn were 2.5 wt% and 2.8 wt%, respectively.

Flow reactor studies.

Reactions of CO_2 and H_2 were performed in a 6 mm o.d. quartz reactor under atmospheric pressure. Approximately 100 mg of catalysts, sieved to 40-60 mesh, were used for steady-state experiments. CO_2, H_2, and Ar (as a diluent) were introduced into the reactor with a constant total flow rate of 40 $mL \cdot min^{-1}$ and a ratio of 1:2:5. The catalysts were heated to 400 ℃ and kept for 14 h for steady-state measurements. Then the reactor was cooled down to lower temperatures with an interval of 10 ℃ to evaluate the activity at different temperatures. The gas products were analyzed online using a gas chromatography (GC), equipped with a flame ionization detector (FID) and a thermal conductivity detector (TCD). Control experiments were carried out using a blank quartz reactor at 400 ℃. Both cases show little activity, indicating that the gas-phase reaction and quartz wool will not strongly affect the reaction. Due to the reducing atmosphere of CO_2 hydrogenation, all catalysts are without reduction treatment and the catalytic data is calculated by averaging data points between 12 and 14 h on stream.

Material characterization.

High-resolution synchrotron X-ray diffraction (XRD) patterns were collected at beamline 17-BM with a wavelength of 0.24128 Å at the advanced photon source (APS) at Argonne National Lab (ANL). Temperature-programmed reduction (TPR) experiments were carried out on the AMI-300ip (Altamira) instrument. For each TPR experiment, approximately 50 mg of the fresh catalyst was put into a U-shaped quartz tube and pre-treated at 300 ℃ for 30 min in a 10% O_2/He flow (50 $mL \cdot min^{-1}$) and then cooled to room temperature. The flow was then switched to a mixture of 10% H_2/Ar with a constant flow rate of 50 $mL \cdot min^{-1}$, and the TPR measurements were performed with a heating rate of 10 $℃ \cdot min^{-1}$ to 800 ℃. The amount of hydrogen consumed as a function of reduction temperature was continuously monitored and recorded by

a TCD, which can be used to compare the reducibility of the catalysts. TEM imaging and EDX elements mapping were performed using a FEI Talos F200X TEM operating at 200 kV. *In-situ* XANES spectra of Ni K-edge (8333 eV) were collected at beamline 2-2 of the Stanford Synchrotron Radiation Lightsource (SSRL). About 50 mg catalyst (60-80 mesh) was loaded into a 3 mm o.d. glassy-carbon tube, packed with quartz wool on both sides of the sample. A reaction gas mixture of CO_2, H_2, and He with a ratio of 1:2:2 (10 $mL \cdot min^{-1}$ in total) was introduced into the reactor. After the spectra being collected at room temperature (fresh state), the reactor was heated to 400 °C with a ramping rate of 20 $°C \cdot min^{-1}$ and hold for 40 min for the collection of XANES spectra during the reaction. All the XANES spectra were taken for three scans. *Ex-situ* XANES spectra of Zn K-edge of the samples were recorded at room temperature using a fluorescence mode at beamline 4B9A of the Beijing Synchrotron Radiation Facility (BSRF), China. To quantify the fraction of Ni-related species of each sample at reaction conditions, the spectra were fitted using the linear combination function in Athena (IFEFFIT 1.2.11 data analysis package). The spectra of Ni foil (Ni^0) and NiO/ZrO_2 (Ni^{2+}) were employed as references for the fitting. *In-situ* diffuse reflectance infrared Fourier transform spectroscopy (DRIFTS) experiments were performed using a FTIR spectrometer (ThermoFisher Nicolet iS 50R FT-IR) equipped with a liquid-N_2 cooled mercury cadmium telluride (MCT) detector. The background spectrum for each sample was recorded at 400 °C after 30 min reduction in a 20 $mL \cdot min^{-1}$ 50% H_2/Ar flow. Following reduction, the *in-situ* DRIFT spectra were recorded at 400 °C in a H_2/CO_2/Ar flow (5 $mL \cdot min^{-1}$ H_2+10 $mL \cdot min^{-1}$ CO_2 + 25 $mL \cdot min^{-1}$ Ar) for 30 min. Then, the reactant gas was switched to 15 $mL \cdot min^{-1}$ H_2 + 25 $mL \cdot min^{-1}$ Ar, while the DRIFT spectra were also collected.

Computational Methods.

Density functional theory (DFT) calculations were performed by the Vienna ab initio simulation (VASP) package. The frozen-core all-electron projector augmented wave (PAW) method was used to describe the electron-ion interaction, in which the generalized gradient approximation with the Perdew-Burke-Ernzerhof (PBE) functional was used to simulate the exchange-correlation energy. The DFT+U method was used for Ni with a Hubbard parameter set to 5.3 eV. During the calculation, an energy cutoff of 400 eV was used. The (111) surface of ZrO_2 was modeled with a 2 × 2 slab, in which the top two layers of atoms and the supported NiO cluster were relaxed. In the relaxation, the force convergence criterion was set to 0.05 eV/Å, and the energy convergence criterion was 10^{-4} eV. The crystal orbital Hamilton population (COHP) method was used to analyze the strength of chemical bonds based on the LOBSTER package.

Acknowledgements

This work was supported by the National Natural Science Foundation of China (NSFC, Grant No. 21978148). The authors thank beamline 4B9A and beamline 1W1B at the Beijing Synchrotron Radiation Facility (BSRF), beamline 17-BM at the Advanced Photon Source (APS), and beamline 2-2 at the Stanford Synchrotron Radiation Lightsource (SSRL) for providing the beam time. The simulations were partly performed on the High-Performance Parallel Computer supported by the UK Engineering and Physical Sciences Research Council under the project UK Consortium on Mesoscale Engineering Sciences (UKCOMES) (Grant No. EP/R029598/1).

Keywords: CO_2 hydrogenation; selectivity; bimetallic effect; NiZn catalysts; Ni-O-Zn site.

References

[1] R. M. Bullock, J. G. Chen, L. Gagliardi, P. J. Chirik, O. K. Farha, C. H. Hendon, C. W. Jones, J. A. Keith, J. Klosin, S. D. Minteer, R. H. Morris, A. T. Radosevich, T. B. Rauchfuss, N. A. Strotman, A. Vojvodic, T. R. Ward, J. Y. Yang, Y. Surendranath, *Science*, **2020**, *369*, eabc3183.

[2] aS. Kattel, P. J. Ramirez, J. G. Chen, J. A. Rodriguez, P. Liu, *Science*, **2017**, *357*; bL. Lin, W. Zhou, R. Gao, S. Yao, X. Zhang, W. Xu, S. Zheng, Z. Jiang, Q. Yu, Y. W. Li, C. Shi, X. D. Wen, D. Ma, *Nature*, **2017**, *544*, 80-83; cS. Yao, X. Zhang, W. Zhou, R. Gao, W. Xu, Y. Ye, L. Lin, X. Wen, P. Liu, B. Chen, E. Crumlin, J. Guo, Z. Zuo, W. Li, J. Xie, L. Lu, C. J. Kiely, L. Gu, C. Shi, J. A. Rodriguez, D. Ma, *Science*, **2017**, *357*, 389-393.

[3] J. K. Nørskov, T. Bligaard, J. Rossmeisl, C. H. Christensen, *Nat. Chem.*, **2009**, *1*, 37-46.

[4] J. G. Chen, R. M. Crooks, L. C. Seefeldt, K. L. Bren, R. M. Bullock, M. Y. Darensbourg, P. L. Holland, B. Hoffman, M. J. Janik, A. K. Jones, M. G. Kanatzidis, P. King, K. M. Lancaster, S. V. Lymar, P. Pfromm, W. F. Schneider, R. R. Schrock, *Science*, **2018**, *360*, eaar6611.

[5] Y. Deng, Y. Ge, M. Xu, Q. Yu, D. Xiao, S. Yao, D. Ma, *Acc. Chem. Res.*, **2019**, *52*, 3372-3383.

[6] aR. Qin, L. Zhou, P. Liu, Y. Gong, K. Liu, C. Xu, Y. Zhao, L. Gu, G. Fu, N. Zheng, *Nat. Catal.*, **2020**, *3*, 703-709; bB. Zhao, P. Zhai, P. Wang, J. Li, T. Li, M. Peng, M. Zhao, G. Hu, Y. Yang, Y.-W. Li, Q. Zhang, W. Fan, D. Ma, *Chem*, **2017**, *3*, 323-333; cW. Tu, C. Sun, Z. Zhang, W. Liu, H. S. Malhi, W. Ma, M. Zhu, Y.-F. Han, *Appl. Catal., B*, **2021**, *298*, 120567.

[7] aS. Kim, B. S. Crandall, M. J. Lance, N. Cordonnier, J. Lauterbach, E. Sasmaz, *Appl. Catal., B*, **2019**, *259*; bM. C. Bacariza, I. Graça, J. M. Lopes, C. Henriques, *ChemCatChem*, **2018**, *10*, 2773-2781.

[8] aY. Song, E. Ozdemir, S. Ramesh, A. Adishev, S. Subramanian, A. Harale, M. Albuali, B. A. Fadhel, A. Jamal, D. Moon, S. H. Choi, C. T. Yavuz, *Science*, **2020**, *367*, 777-781; bF. Studt, F. Abild-Pedersen, T. Bligaard, R. Z. Sorensen, C. H. Christensen, J. K. Norskov, *Science*, **2008**, *320*, 1320-1322; cC. Zhang, M. Xu, Z. Yang, M. Zhu, J. Gao, Y.-F. Han, *Appl. Catal., B*, **2021**, *295*, 120287.

[9] K. D. Gilroy, A. Ruditskiy, H. C. Peng, D. Qin, Y. Xia, *Chem. Rev.*, **2016**, *116*, 10414-10472.

[10] Y. Cao, Z. Sui, Y. Zhu, X. Zhou, D. Chen, *ACS Catal.*, **2017**, *7*, 7835-7846.

[11] K. Liu, R. Qin, N. Zheng, *J. Am. Chem. Soc.*, **2021**, *143*, 4483-4499.

[12] Z. Xie, D. Tian, M. Xie, S.-Z. Yang, Y. Xu, N. Rui, J. H. Lee, S. D. Senanayake, K. Li, H. Wang, S. Kattel, J. G. Chen, *Chem*, **2020**, *6*, 2703-2716.

[13] aB. H. Yan, B. H. Zhao, S. Kattel, Q. Y. Wu, S. Y. Yao, D. Su, J. G. G. Chen, *J. Catal.*, **2019**, *374*, 60-71; bB. Yan, S. Yao, S. Kattel, Q. Wu, Z. Xie, E. Gomez, P. Liu, D. Su, J. G. Chen, *Proc. Natl. Acad. Sci. U.S.A.*, **2018**, *115*, 8278-8283; cC. Zhang, C. Cao, Y. Zhang, X. Liu, J. Xu, M. Zhu, W. Tu, Y.-F. Han, *ACS Catal.*, **2021**, *11*, 2121-2133; dY. Zhu, S. F. Yuk, J. Zheng, M. T. Nguyen, M. S. Lee, J. Szanyi, L. Kovarik, Z. Zhu, M. Balasubramanian, V. A. Glezakou, J. L. Fulton, J. A. Lercher, R. Rousseau, O. Y. Gutierrez, *J. Am. Chem. Soc.*, **2021**, *143*, 5540-5549.

[14] M. G. Sibi, D. Verma, H. C. Setiyadi, M. K. Khan, N. Karanwal, S. K. Kwak, K. Y. Chung, J.-H. Park, D. Han, K.-W. Nam, J. Kim, *ACS Catal.*, **2021**, 8382-8398.

[15] aF. Rubio-Marcos, C. V. Manzano, J. J. Reinosa, J. J. Romero, P. Marchet, M. S. Martín-González, J. F. Fernández, *J. Phys. Chem. C*, **2011**, *115*, 13577-13583; bK. J. Gaskell, A. Starace, M. A. Langell, *J. Phys. Chem. C*, **2007**, *111*, 13912-13921; cC. S. Spanjers, R. S. Sim, N. P. Sturgis, B. Kabius, R. M. Rioux, *ACS Catal.*, **2015**, *5*, 3304-3315.

[16] aB. Zhao, B. Yan, Z. Jiang, S. Yao, Z. Liu, Q. Wu, R. Ran, S. D. Senanayake, D. Weng, J. G. Chen, *Chem. Commun.*, **2018**, *54*, 7354-7357; bK. Feng, J. Tian, M. Guo, Y. Wang, S. Wang, Z. Wu, J. Zhang, L. He,

B. Yan, *Appl. Catal., B*, **2021**, *292*, 120191.

[17] aJ. Wang, G. Li, Z. Li, C. Tang, Z. Feng, H. An, H. Liu, T. Liu, C. Li, *Sci. Adv.*, **2017**, *3*, e1701290; bJ. Wang, C. Tang, G. Li, Z. Han, Z. Li, H. Liu, F. Cheng, C. Li, *ACS Catal.*, **2019**, *9*, 10253-10259.

[18] aJ.-A. Dalmon, M. Primet, G.-A. Martin, B. Imelik, *Surf. Sci.*, **1975**, *50*, 95-108; bG. Blyholder, *J. Phys. Chem.*, **1964**, *68*, 2772-2777.

Entry for the Table of Contents

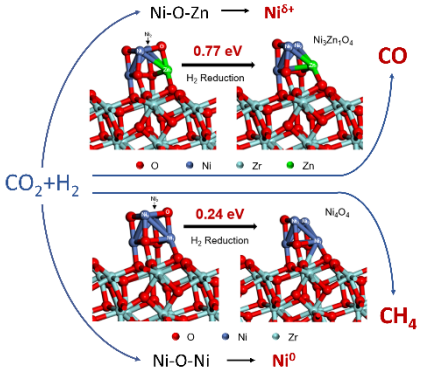

For CO_2 hydrogenation over NiZn/ZrO_2 catalysts, Zn is atomically dispersed in the phase of NiO and ZrO_2 in form of $NiZnO_x$ and $ZnZrO_x$, respectively. The formed Ni-O-Zn sites enhance the bonding strength of Ni to the ligand O, stabilizing the Ni species with positive charge ($Ni^{\delta+}$) under reduction atmosphere. The $Ni^{\delta+}$ species weaken the adsorption and hydrogenation capacity of adsorbed CO and thereafter promote the reverse water gas shift (RWGS) reaction.